AGU PUBLICATIONS

JGR

Journal of Geophysical Research: Atmospheres

RESEARCH ARTICLE
10.1002/2015JD023480

Key Points:
- Parameterization of imaged particles enables quantification of mixing state
- Two major mixing states were observed in Sacramento
- Mixing state parameterization is dependent on analytical technique

Supporting Information:
- Text S1, Figure S1, and Tables S1 and S2
- Table S3
- Table S4
- Table S5
- Table S6
- Table S7
- Table S8

Correspondence to:
R. C. Moffet,
rmoffet@pacific.edu

Citation:
O'Brien, R. E., et al. (2015), Chemical imaging of ambient aerosol particles: Observational constraints on mixing state parameterization, *J. Geophys. Res. Atmos.*, *120*, 9591–9605, doi:10.1002/2015JD023480.

Received 17 APR 2015
Accepted 23 AUG 2015
Accepted article online 26 AUG 2015
Published online 28 SEP 2015

Chemical imaging of ambient aerosol particles: Observational constraints on mixing state parameterization

Rachel E. O'Brien[1,2,3], Bingbing Wang[4], Alexander Laskin[4], Nicole Riemer[5], Matthew West[6], Qi Zhang[7], Yele Sun[7], Xiao-Ying Yu[8], Peter Alpert[9,10], Daniel A. Knopf[9], Mary K. Gilles[2], and Ryan C. Moffet[1]

[1]Department of Chemistry, University of the Pacific, Stockton, California, USA, [2]Lawrence Berkeley National Laboratory, Berkeley, California, USA, [3]Now at Department of Civil and Environmental Engineering, Massachusetts Institute of Technology, Cambridge, Massachusetts, USA, [4]William R. Wiley Environmental and Molecular Sciences Laboratory, Pacific Northwest National Laboratory, Richland, Washington, USA, [5]Department of Atmospheric Sciences, University of Illinois at Urbana-Champaign, Urbana, Illinois, USA, [6]Department of Mechanical Science and Engineering, University of Illinois at Urbana-Champaign, Urbana, Illinois, USA, [7]Department of Environmental Toxicology, University of California, Davis, California, USA, [8]Fundamental and Computational Sciences Directorate, Pacific Northwest National Laboratory, Richland, Washington, USA, [9]Institute for Terrestrial and Planetary Atmospheres, School of Marine and Atmospheric Sciences, Stony Brook University, Stony Brook, New York, USA, [10]Now at Institut de Recherches sur la Catalyse et l'Environnement de Lyon, Centre National de la Recherche Scientifique, Université Claude Bernard Lyon 1, Villeurbanne, France

Abstract A new parameterization for quantifying the mixing state of aerosol populations has been applied for the first time to samples of ambient particles analyzed using spectro-microscopy techniques. Scanning transmission X-ray microscopy/near edge X-ray absorption fine structure (STXM/NEXAFS) and computer-controlled scanning electron microscopy/energy dispersive X-ray spectroscopy (CCSEM/EDX) were used to probe the composition of the organic and inorganic fraction of individual particles collected on 27 and 28 June during the 2010 Carbonaceous Aerosols and Radiative Effects study in the Central Valley, California. The first field site, T0, was located in downtown Sacramento, while T1 was located near the Sierra Nevada Mountains. Mass estimates of the aerosol particle components were used to calculate mixing state metrics, such as the particle-specific diversity, bulk population diversity, and mixing state index, for each sample. The STXM data showed evidence of changes in the mixing state associated with a buildup of organic matter confirmed by collocated measurements, and the largest impact on the mixing state was due to an increase in soot dominant particles during this buildup. The mixing state from STXM was similar between T0 and T1, indicating that the increased organic fraction at T1 had a small effect on the mixing state of the population. The CCSEM/EDX analysis showed the presence of two types of particle populations: the first was dominated by aged sea-salt particles and had a higher mixing state index (indicating a more homogeneous population); the second was dominated by carbonaceous particles and had a lower mixing state index.

1. Introduction

Atmospheric aerosols affect the atmospheric environment and climate directly by absorbing and scattering radiation and indirectly by impacting the properties and lifetimes of clouds [*Poschl*, 2005; *Solomon et al.*, 2007]. Atmospheric aerosol particles consist of a mixture of organic molecules, inorganic salts, metals, and elemental carbon or soot [*Seinfeld and Pandis*, 2006]. Their optical and cloud formation properties depend on particle-specific composition and on particle morphology (i.e., how the particle's constituents are arranged within the particle) [*Jacobson et al.*, 2000; *Kanakidou et al.*, 2005; *Petters and Kreidenweis*, 2007; *Knopf et al.*, 2010; *Wang et al.*, 2012; *Knopf et al.*, 2014]. For example, organics coated on soot have been shown to increase the absorption coefficient in some cases or negligible effect in others [*Schnaiter et al.*, 2005; *Mikhailov et al.*, 2006; *Moffet and Prather*, 2009; *Cappa et al.*, 2012; *Bond et al.*, 2013].

An important term in this context is the so-called *population mixing state*, which we use here to describe how chemical species are distributed over the entire particle population. Note that this definition is purely based on composition and does not include any features of particle morphology. Traditionally, the terms "external mixture" and "internal mixture" have been used to characterize the population mixing state. An external mixture consists of single-component particles, i.e., particles that contain only one species. In contrast, an internal mixture refers to a population that contains multicomponent particles. *Riemer and West* [2013] argued that

these terms fall short of a meaningful characterization of ambient aerosol populations, since observations have shown that even freshly emitted aerosol populations can be to some extent internal mixtures (e.g., sea spray aerosol, multicomponent mineral dust, or particles from combustion sources) and that these internal mixtures then evolve further in the atmosphere due to condensation of gas-phase organics or inorganics onto existing particles [*Johnson et al.*, 2005; *Moffet et al.*, 2010b; *Wang et al.*, 2010; *Moffet et al.*, 2013], due to chemical transformations within the particles [*Laskin et al.*, 2012], or due to coagulation events between particles [*Jacobson*, 2001]. Associated with the changes in mixing state are changes in hygroscopicity and optical properties [*Cappa et al.*, 2012; *Lack et al.*, 2012; *Saleh et al.*, 2014].

To better quantify population mixing state, and to enable us to tie it to observed changes in the physical properties, *Riemer and West* [2013] proposed a new parameterization based on diversity measures. This parameterization uses the particle-specific mass fractions of the aerosol components to calculate two measures of diversity: a population-level bulk diversity and an average particle-specific diversity. The population mixing state index can then be defined from an affine ratio of these two fundamental quantities. It is straightforward to apply this parameterization to single-particle analysis techniques that allow measurement of the masses of individual components in aerosol particles. *Healy et al.* [2014] have applied this parameterization to data collected using a single particle mass spectrometer, an aerosol mass spectrometer, a scanning mobility particle sizer, and a multiangle absorption photometer. With these instruments, singe-particle mass estimates for black carbon, organics, sulfate, nitrate, and ammonia were used to quantify the aerosol mixing state during the MEGAPOLI 2010 campaign in Paris, France. They measured different particle compositions for aerosols from different sources (e.g., wood burning versus aged carbonaceous) and showed a characteristic diurnal cycle and a dependence on the origin of the air mass for the mixing state metrics.

In this paper, we analyze the composition of individual particles using scanning transmission X-ray microscopy/near edge X-ray absorption fine structure (STXM/NEXAFS) spectroscopy and computer-controlled scanning electron microscopy/energy dispersive X-ray spectroscopy (CCSEM/EDX). These techniques have been applied in many studies to characterize the composition, the size, and the different types of aerosol particles from field campaigns [*Laskin et al.*, 2006; *Moffet et al.*, 2010a, 2010b; *Laskin et al.*, 2012; *Wang et al.*, 2012; *Moffet et al.*, 2013; *Knopf et al.*, 2014]. STXM/NEXAFS is a chemical imagining technique that uses absorption of X-rays at specific energies to map the composition of individual aerosol particles with a spatial resolution of about 30 nm. STXM/NEXAFS at the carbon K-edge can be used to quantify the amount of organic, inorganic, and soot in the particles, making it well suited for the quantification of the carbonaceous fraction. CCSEM/EDX can be used to measure the elemental composition of individual particles by collecting the X-ray emission spectrum from each particle. Thus, analysis by CCSEM/EDX provides complementary information on the composition of the inorganic fraction at the elemental level.

The Carbonaceous Aerosol and Radiative Effects Study (CARES) took place in June 2010 in Central Valley, California. One of the primary objectives was to study the evolution of atmospheric aerosols during aging and transport. Two ground sites were set up, one in downtown Sacramento (T0) and a second about 40 km to the northeast in the Sierra Nevada foot hills (T1) [*Zaveri et al.*, 2012]. In this study, we present results on the application of this novel mixing state parameterization to populations of atmospheric particles sampled during the CARES 2010 field study at each of the two ground sites and analyzed using both STXM/NEXAFS [*Moffet et al.*, 2011] and CCSEM/EDX [*Laskin et al.*, 2006].

2. Experimental Procedure

2.1. Sample Collection/Data Analysis

A description of the sample and data collection is given elsewhere [*Moffet et al.*, 2013]. Briefly, samples were collected on 27 and 28 June in 15 min intervals at both the Sacramento T0 site (38°38′55.55″, 121°20′59.02″) and the Cool T1 site (38°52′17.02″, 121°1′21.59″) using time-resolved aerosol collectors. This sampler has an effective cutoff size, d_{50} (diameter of particles collected with 50% efficiency), of 0.36–0.38 mm [*Laskin et al.*, 2003], and samples were impacted onto either copper-grid-supported carbon B films or silicon nitride windows. Table 1 lists specific times of eleven samples from the T0 site and 9 samples from T1 site analyzed for this study using STXM/NEXAFS. Some samples contained less than 300 particles but had another data set collected during the same hour. To improve statistics, these data sets were combined as indicated in Table 1.

Table 1. Sample Times (Site_Day_Start Time), Particle Class Statistics, and Mixing State Parameters for Samples Analyzed With STXM/NEXAFS

Sample	OC	INECOC	ECOC	INOC	Total Particles	D_α	D_γ	χ (%)
T0_27_10:27	85	13	5	232	335	1.8	1.9	83
T0_27_12:27	52	150	18	590	810	1.9	1.9	91
T0_27_13:07	57	73	23	340	493	1.9	2.2	80
T0_27_20:28	169	18	20	167	374	1.9	2.1	80
T0_28_05:49	88	186	46	926	1246	1.9	2.1	86
T0_28_08:09	136	84	32	350	602	2.0	2.4	72
T0_28_13:09	303	88	40	588	1019	2.0	2.2	80
T0_28_15:30	550	176	120	828	1674	2.0	2.6	62
T0_28_20:10	55	126	13	857	1051	1.8	1.9	90
T0_28_22:00[a]	61	90	23	644	818	1.7	1.8	89
T0_28_23:31	13	49	8	324	394	1.7	1.7	93
T1_27_07:01	264	21	25	243	553	1.9	2.2	77
T1_27_12:22	275	41	27	500	843	1.9	2.0	88
T1_27_13:35	159	66	21	324	570	2.0	2.1	86
T1_27_14:55	370	22	53	216	661	1.9	2.0	88
T1_27_23:36	248	24	24	273	569	1.9	2.0	89
T1_28_6:57	120	69	29	347	565	2.0	2.2	84
T1_28_11:37	630	121	80	642	1473	1.9	2.2	77
T1_28_14:18	645	120	81	688	1534	2.0	2.2	83
T1_28_16:00[a]	185	77	33	201	496	2.1	2.4	78

[a]Three samples (T0_28_22:00) and two samples (T1_28_16:00) collected during the given hour were combined for analysis.

Samples collected during the same 2 days, but not collected at the same times as the ones analyzed with STXM/NEXAFS, were analyzed with CCSEM/EDX (Table 2). All times are given in local standard time.

The STXM/NEXAFS measurements were taken at the Advanced Light Source at Lawrence Berkeley National Laboratory on beamlines 11.0.2 and 5.3.2.2. The operation of the microscope has been explained in detail elsewhere [*Kilcoyne et al.*, 2003]. Briefly, a Fresnel zone plate was used to focus energy selected X-ray light to a 30–35 nm spot size, while the sample was raster scanned at the focal point. Transmitted X-rays were detected producing an image at a given photon energy. The light from sample free regions provided the reference intensity (I_0) and the light that was transmitted through the particles is the sample intensity (I). The transmitted signal was converted to optical density (OD) using:

$$\mathrm{OD} = \ln(I/I_0) = \mu\rho t \quad (1)$$

Table 2. Sample Times (Site_Day_Start Time), Particle Type Statistics, and Mixing State Parameters for Samples Analyzed With CCSEM/EDX

Sample	Sea Salt	Sea Salt/Sulfates	Carbonaceous	Other	Total Particles	D_α	D_γ	χ (%)
T0_27_11:47	2150	46	126	22	2344	3.2	3.6	86
T0_27_14:27	2998	149	258	24	3429	3.0	3.3	86
T0_27_16:27	305	116	2601	167	3189	2.0	3.3	44
T0_27_18:07	71	59	2331	101	2562	1.6	2.1	57
T0_27_19:48	710	176	2348	171	3405	1.9	2.9	49
T0_28_06:49	598	52	124	18	792	2.5	3.1	70
T0_28_07:29	1229	22	46	22	1319	3.8	4.1	91
T0_28_14:29	460	133	1285	33	1911	1.8	2.6	52
T1_27_08:01	400	228	3180	415	4223	1.9	3.2	40
T1_27_12:02	608	280	4482	455	5825	2.0	3.3	45
T1_27_16:15	913	283	3677	149	5022	1.9	2.8	54
T1_27_19:36	156	102	945	42	1245	1.9	2.6	58
T1_27_21:10	136	73	1358	53	1620	2.0	2.7	59
T1_28_6:17	84	111	989	56	1240	1.9	2.5	60
T1_28_17:38	25	44	430	76	575	2.4	3.5	56
T1_28_18:18	10	24	237	28	299	2.1	2.6	65

where μ is the mass absorption coefficient, ρ is the density, and t is the sample thickness. The X-ray photon energy was then incremented to produce either a stack of images or four energy maps (278, 285.4, 288, and 320 eV) [*Moffet et al.*, 2013]. The work presented here uses analysis of images collected at the carbon K-edge (278 eV to 320 eV). Three component types were identified in the particles following the procedures of *Moffet et al.* [2010a]. Briefly, pixels with OD_{320}-OD_{278} (postedge minus preedge) greater than zero were identified as organic (OC); pixels with OD_{278}/OD_{320} greater than 0.5 were identified as inorganic (IN); finally, pixels with sp^2 carbon greater than 35% were identified as black carbon or soot (BC). Here the term BC (instead of the previously used elemental carbon or EC) will be used to describe soot containing pixels to match the notation used in the modeling community [*Bond et al.*, 2013; *Riemer and West*, 2013]. STXM/NEXAFS analysis was performed over 8816 particles from the samples collected at T0 and 7264 particles from the samples collected at T1 (Table 1).

The CCSEM/EDX measurements were taken at the Environmental Molecular Science Laboratory using an FEI Quanta digital field emission gun environmental SEM. In this work, X-ray spectra for particles with circular diameter larger than 0.1 μm were used. The spectra were acquired at an accelerating voltage of 20 kV with a beam current of 500 pA. The elements used for the identification of the particle type were C, N, O, Na, Mg, Al, Si, P, S, Cl, K, Ca, Mn, Fe, and Zn. For the mixing state analysis carbon, nitrogen, and oxygen were excluded from the calculations (for details, see Discussion). CCSEM/EDX analysis was performed on over 18,951 particles from the samples collected at T0 and over 20,049 particles from the samples collected at T1 (Table 2).

2.2. Parameterization Methodology

The mixing state parameterization has been described in detail by *Riemer and West* [2013]. For clarity, the terminology and calculations from that paper are reproduced here. The diversity analysis is based on the species mass fractions in a particle and in the population. For a given species a in a particle i, the mass of species a is termed μ_i^a, where $a = 1,\ldots, A$ and $i = 1,\ldots, N$. The mass of a particle i is the sum of the mass of each species present in that particle:

$$\mu_i = \sum_{a=1}^{A} \mu^a{}_i \tag{2}$$

The total mass of particle population, μ, is then a summation of the μ_i for all the particles in that population. The mass fraction of a particle i in the population (p_i) is given by

$$p_i = \frac{\mu_i}{\mu} \tag{3}$$

The mass fraction of species a in a particle i (p_i^a) is given by

$$p^a{}_i = \frac{\mu^a{}_i}{\mu_i} \tag{4}$$

Finally, the mass fraction of species a in the population is given by

$$p^a = \frac{\mu^a}{\mu} \tag{5}$$

Details on the mass calculations for both the STXM and CCSEM data sets are provided in the following section. Using the mass fractions calculated in equations (3)–(5), the Shannon entropy [*MacKay*, 2003] for each particle (H_i), for the average per particle (H_α), and for the bulk population (H_γ) can be calculated using equations (6)–(8), respectively:

$$H_i = \sum_{a=1}^{A} -p^a{}_i \ln p^a{}_i \tag{6}$$

$$H_\alpha = \sum_{i=1}^{N} p_i H_i \tag{7}$$

$$H_\gamma = \sum_{a=1}^{A} -p^a \ln p^a \tag{8}$$

The Shannon entropy can be physically regarded as an information measure of the uniformity of the mass fractions, with low entropy indicating nonuniform mass fractions across the particle population and the

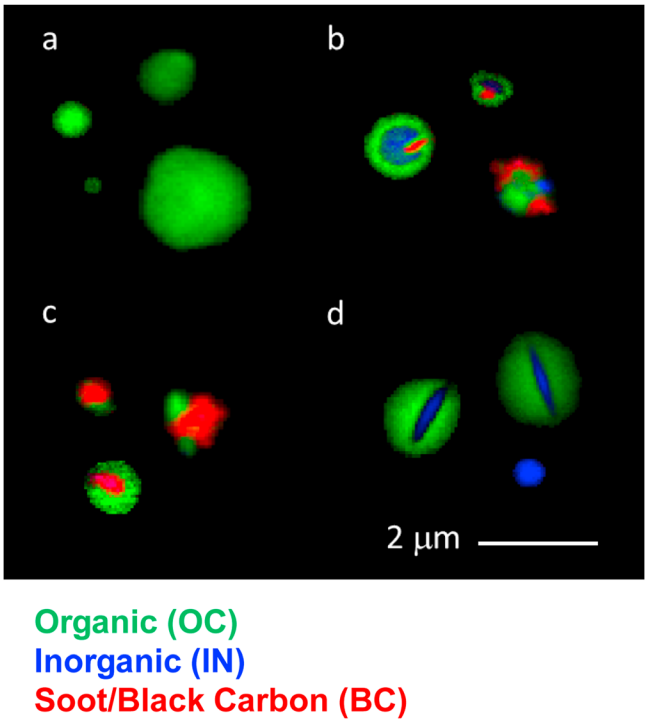

Figure 1. STXM/NEXAFS particle classification for T0 and T1. (a–d) Singular value decomposition maps (green = OC, red = BC, blue = IN) of representative particles from the four classes: type 1: OC (Figure 1a), type 2: OCBCIN (Figure 1b), type 3: OCBC (Figure 1c), and type 4: OCIN (Figure 1d).

highest entropy being achieved for completely uniform mass fractions. For further details, see *Riemer and West* [2013].

The particle diversity (D_i) is then calculated by taking the exponent of the particle-specific Shannon entropy H_i (equation (6)). D_i can be interpreted as the "effective number of species" in the particle and can range from 1 (the particle contains a single pure component) to A (the particle has equal mass fractions of all A components). Similarly, the average particle-specific diversity (D_α) and the bulk population diversity (D_γ) are calculated by taking the exponent of the corresponding Shannon entropy values, H_α and H_γ, respectively. The mixing state index χ is then defined as

$$\chi = \frac{D_\alpha - 1}{D_\gamma - 1} \tag{9}$$

where D_α and D_γ can range from 1 to A. By construction, the bulk diversity D_γ is always greater than or equal to the average particle-specific diversity D_α. Thus, the mixing state index, χ, can range from 0% for an external mixture (heterogeneous population consisting of single-component particles) to 100% when D_α equals D_γ (homogeneous population with all particles having identical compositions, equal to the composition of the bulk). The STXM data sets contain three components (organic, inorganic, and black carbon) so D_i, D_α, and D_γ can range from 1 to 3. In the CCSEM data sets there are 12 different elements, so the diversity values can range from 1 to 12.

2.3. Mass Calculations

The STXM data set contains (1) the two-dimensional size of the impacted particles, (2) the identified components at each pixel in the particles, and (3) the optical density at each pixel for all of the photon energies measured. Figure 1 shows singular value decomposition maps of representative particles. Three component types were identified in the particles: organic (OC, green), inorganic (IN, blue), and black carbon (BC, red). Since STXM measures the absorption through the particle, each pixel in a particle can contain 1 to 3 components (i.e., components stacked on top of each other). For the mass estimates, a thickness was calculated from the average optical densities at 278 eV and 320 eV over each particle as described below. For the soot calculations, only pixels labeled BC were included, and all carbon in those pixels was assumed to be soot. For the organic calculations, all pixels that were labeled OC (excluding pixels that contained both a BC and an OC label) were used.

To estimate the thickness of carbon and inorganic components, the optical densities (OD) at 320 and 278 eV were used. For atmospheric particles, the OD at a given energy is estimated as a linear combination of the ODs of the inorganic and organic components:

$$\mathrm{OD}_{320} = \mu_{\mathrm{in},320}\rho_{\mathrm{in}}t_{\mathrm{in}} + \mu_{\mathrm{org},320}\rho_{\mathrm{org}}t_{\mathrm{org}} \tag{10}$$

$$\mathrm{OD}_{278} = \mu_{\mathrm{in},278}\rho_{\mathrm{in}}t_{\mathrm{in}} + \mu_{\mathrm{org},278}\rho_{\mathrm{org}}t_{\mathrm{org}} \tag{11}$$

By taking OD_{320}-OD_{278}, the thickness of the inorganic (t_{in}) and organic (t_{org}) components can be calculated as

$$t_{in} = \frac{OD_{278} - \mu_{org,278}\rho_{org}t_{org}}{\mu_{in,278}\rho_{in}} \quad (12)$$

$$t_{org} = \frac{OD_{320} - \left(\left(\mu_{in,320}/\mu_{in,278}\right)OD_{278}\right)}{\left(\mu_{org,320} - \left(\mu_{in,320} \times \mu_{org,278}/\mu_{in,278}\right)\right)\rho_{org}} \quad (13)$$

The mass absorption coefficients (μ) for both inorganic and organic components were calculated using the same method as *O'Brien et al.* [2014] using an average O/C value of 0.4 [*Setyan et al.*, 2012] and assuming that the dominant inorganic component was ammonium sulfate: $\mu_{in,320} = 11{,}460\ cm^2/g$, $\mu_{in,278} = 15{,}230\ cm^2/g$, $\mu_{org,320} = 22{,}500\ cm^2/g$, $\mu_{org,278} = 1{,}100\ cm^2/g$ [*Henke et al.*, 1993]. For soot, an average O/C of 0.3 was assumed [*Hopkins et al.*, 2007; *Zelenay et al.*, 2011] and $\mu_{org,320} = 29{,}556\ cm^2/g$, $\mu_{org,278} = 3{,}095\ cm^2/g$ were used. The known density for ammonium sulfate ($1.77\ g/cm^3$) was used for the inorganic. Densities of $1.3\ g/cm^3$ [*Setyan et al.*, 2012] and $1.8\ g/cm^3$ [*Bond and Bergstrom*, 2006] were used for the average densities of the organic and soot components, respectively. The particle-specific volume of each component was determined by multiplying the calculated thickness by the area of either the inclusion (black carbon), the impacted particle (inorganic), or the area of the impacted particle minus the area of the soot inclusion (organic). A mass was then calculated by multiplying by the corresponding densities given above.

Ammonium sulfate was assumed to be the dominant inorganic in the particles analyzed with STXM/NEXAFS. During the CARES campaign, the dominant nonrefractory particle component, after organics, was sulfate followed by nitrate and ammonium [*Zaveri et al.*, 2012], indicating that ammonium sulfate and ammonium nitrate were present in particles during the campaign. However, since both STXM/NEXAFS and CCSEM/EDX analyses were run under vacuum (~0.5–20 mTorr), the ammonium nitrate content is expected to be small given its high volatility [*Richardson and Hightower*, 1987].

The CCSEM/EDX data set contains two-dimensional areas of the particles and elemental atomic percentages. Following a particle-type classification scheme similar to that in *Laskin et al.* [2012], particles were separated into groups of aged sea salt, aged sea salt with sulfate, carbonaceous, and other. To estimate the mass of each particle (μ_i = density × volume), the particles were assumed to be hemispheres and densities were assigned by group: $2.0\ g/cm^3$ for the aged sea-salt particles (with and without sulfate) and "other" particles and $1.3\ g/cm^3$ for carbonaceous particles. To calculate the mass of each element, the elemental percent (elemental%) was changed to a weight percent, which was multiplied by the estimated particle mass to calculate the mass fraction:

$$\mu^a{}_i = \mu_i \left(\frac{\text{elemental\%}^a \times \text{molar mass}^a}{\sum_{a=1}^{A} \text{elemental\%}^a \times \text{molar mass}^a}\right) \quad (14)$$

The area equivalent diameter of each particle was calculated for particles from both STXM/NEXAFS and CCSEM/EDX data sets. For analyses as a function of particle size, the data were binned in 0.1 μm steps and the mass and particle-specific diversity values were averaged over each size bin.

3. Results and Discussion

3.1. Carbonaceous Mixing State by STXM

3.1.1. Component Masses and Particle Diversities

From the STXM/NEXAFS data, the mass fractions of the inorganic (IN), the organic carbon (OC), and the black carbon or soot (BC) components were estimated as described above. Similar to previous analyses [*Moffet et al.*, 2010a, 2010b; *Moffet et al.*, 2013], four different particle classes were identified (Figure 1). Figures 1a–1d show homogeneous organic particles (OC) (Figure 1a), organic particles with both inorganic and soot inclusions (INBCOC) (Figure 1b), organic particles with soot inclusions (BCOC) (Figure 1c), and particles that are organic with inorganic inclusions and/or inorganic dominant areas (INOC) (Figure 1d). All of the particles observed contained some organic and inorganic mass. Thus, the difference between particles on the left in Figures 1a and 1c versus the right in Figures 1b and 1d is morphology based. The particles in Figures 1b and 1d have the inorganic

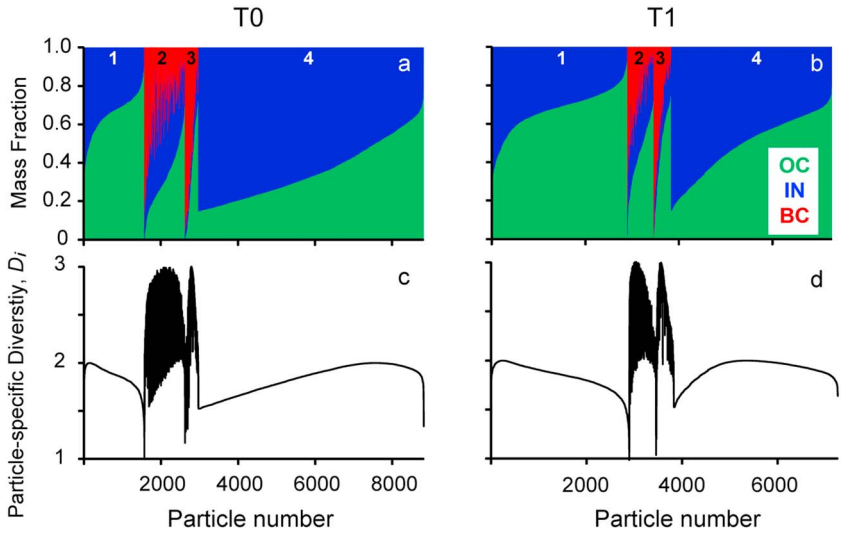

Figure 2. Mass fractions of organic (OC, green), inorganic (IN, blue), and black carbon (BC, red) per (a and b) particle; (c and d) particle-specific diversity, D_i, for CARES T0 (Figures 2a and 2c) and T1 (Figures 2b and 2d). In Figures 2a–2d) particles are grouped by particle types: (1) OC, (2) INBCOC, (3) BCOC, and (4) INOC. Each mass fraction bar (Figures 2a and 2b) and data point (Figures 2c and 2d) correspond to an individual particle (bars and points are not resolvable). The particles are sorted by increasing organic mass in each group.

mass either as an inclusion or as the dominant component in a region of the particle, while the particles in Figures 1a and 1c have the inorganic either homogeneously mixed with the organic or as inclusions that are smaller than the resolution limit of the STXM.

Figures 2a and 2b show the mass fractions of the three components in the analyzed particles from T0 (Figure 2a) and T1 (Figure 2b) samples, respectively. This figure is a pictorial representation of the particle-specific diversity, D_α, over the populations at both T0 and T1. The data are separated by the different particle types listed previously (indicated by the labels 1 to 4). Overall, the organic mass fraction for particles within each of the four types was higher for T1 than T0. This is consistent with an increase in organic mass through both condensation of organics onto INOC particles and more nucleation and growth of new OC particles at T1 [*Setyan et al.*, 2014]. A similar conclusion was reached from analysis of the total organic carbon per particle as a function of particle size on a subset of these data [*Moffet et al.*, 2013].

Figures 2c and 2d show the corresponding particle-specific diversity (D_i), or the effective number of species, in all analyzed particles from T0 (Figure 2c) and T1 (Figure 2d). The particles are plotted in the same order as Figures 2a and 2b. For a particle with a single component, D_i will be 1. A maximum diversity occurs when a particle contains equal mass fractions of all components. In the OC and INOC particles (types 1 and 4, respectively) the diversities range from 1 to 2 with the majority of the particles in these two classes having diversities between 1.5 and 2 (average $D_i = 1.8$). Particles from types 2 (INBCOC) and 3 (BCOC) have diversities that range from 1 to 3 with the majority of the particles having diversities larger than 2. Overall, less than 0.1% (at T0) and 0.2% (at T1) of the particles have D_i values less than 1.3. The majority of the particles have diversity values between the minimum and maximum values, indicating that the particle populations at T0 and T1 were neither minimally nor maximally diverse in their constituents.

3.1.2. STXM: Carbonaceous Mixing State Time Series

Figure 3 shows a time series of the mixing state parameters for particles from T0 (Figure 3a) and T1 (Figure 3b) with the average particle-specific diversity, D_α (blue); the bulk diversity, D_γ (black); and the mixing state index, χ (red). The error bars correspond to an analysis using a mixed inorganic with ratios of 6:2:3:1 of $(NH_4)_2SO_4$, Na_2SO_4, NH_4NO_3, and $NaNO_3$, respectively. These ratios were estimated using data from Aerosol Mass Spectrometers (AMS) [*Setyan et al.*, 2012] and Particle into Liquid Samplers (PILS) [*Zaveri et al.*, 2012] collocated at both field sites (see supporting information for details on this calculation). These inorganic fractions are not the proposed average inorganic aerosol particle composition. Instead, they are used to provide an upper bound on the error based on collocated measurements of the inorganic fraction.

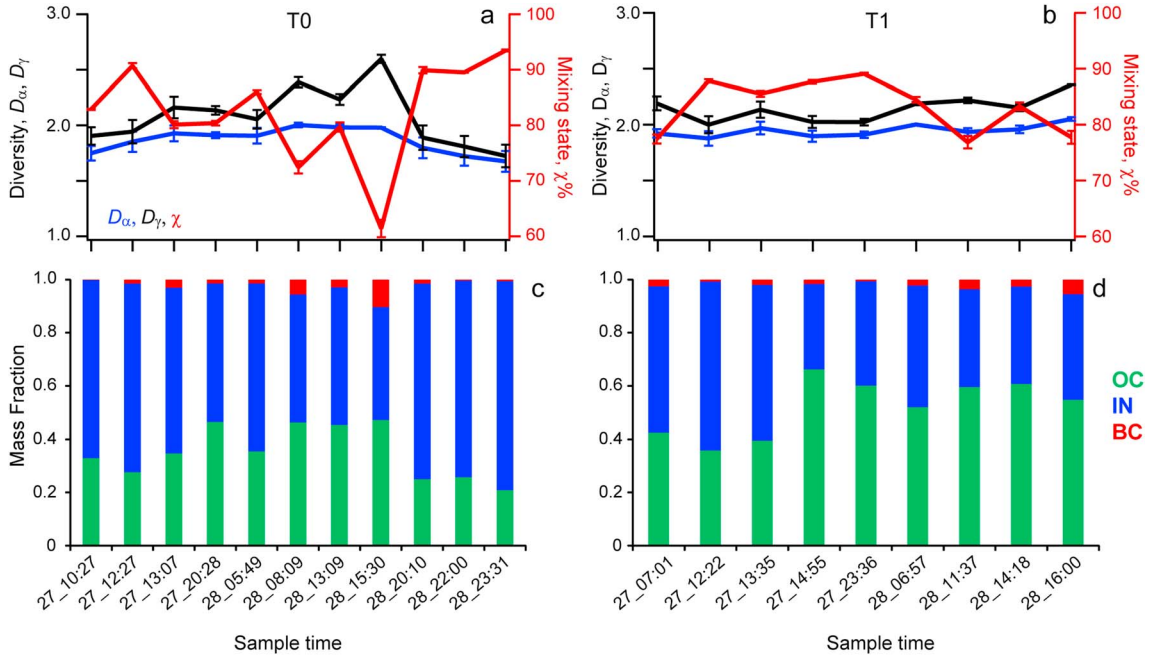

Figure 3. Average particle-specific, D_α (blue), and bulk, D_γ (black), population diversities and mixing state index values (red) for (a) T0 and (b) T1. Error bars correspond to the analysis using ratios of 6:2:3:1 for a mixture of $(NH_4)_2SO_4$, Na_2SO_4, NH_4NO_3, and $NaNO_3$ as the inorganic in mass calculations. Bulk mass fractions for each sample at (c) T0 and (d) T1.

Given that *Setyan et al.* [2012] found that at T1 most of the nitrate signal was likely organic nitrates, the actual amount of inorganic nitrate in the particles was likely lower during the campaign.

In Figure 3, at T0 the particle populations showed a small increase in D_α and a larger increase in D_γ up through the afternoon of the 28 June (15:30) followed by a small decrease in D_α and a larger decrease in D_γ. Since the average particle-specific diversity, D_α, did not fluctuate significantly, the changes observed in the bulk diversity, D_γ, drive the observed changes in the mixing state, χ. Thus, at T0, the mixing state index of the particle populations generally decreased through the afternoon of the 28 June (15:30) and then increased again in the last three samples. Smaller changes with time were observed at the T1 field site.

The time period reported here corresponds to an event of substantially increased organic aerosol mass observed at both T0 and T1 [*Setyan et al.*, 2012; *Moffet et al.*, 2013]. These 2 days had the highest O_3 mixing ratios (70–80 ppb) and the highest daily average temperatures of the campaign, indicating that some of the increase in organic mass was likely due to increased emissions of precursors and more intense atmospheric processing [*Setyan et al.*, 2012]. Measurements with a collocated Sunset ECOC analyzer showed that the organic mass at T0 increased through the afternoon of the 28 June and then dropped at around 17:00 [*Moffet et al.*, 2013]. At T0, organic mass fractions were positively correlated with the OC measurements from the Sunset ECOC with $R^2 = 0.56$. The soot mass fractions at T0 also correlated well with the soot (EC) measurements from the Sunset ECOC with a positive slope and R^2 of 0.82 (Figure S1 in the supporting information).

During the time of this organic mass build up, the particle population became more heterogeneous (the mixing state index decreased). During this event, two effects were taking place: (1) an increase in the BC mass fraction and (2) a small increase in the mass fraction of the organic (Figures 3c and 3d). The increase in the BC mass fraction at T0 increased the D_γ value (bulk population closer to equal mass fractions). This is similar to the archetypal "case 1" discussed in *Riemer and West* [2013], where addition of black carbon to an initial particle population lowered the particle-specific diversity and increased the bulk population diversity. The net effect was a decrease in the mixing state index (the population became more heterogeneous). The second change, a small increase in the organic mass, is similar to the archetypal "case 5" from *Riemer and West* [2013], where condensation onto a population increased both D_α and D_γ, resulting in a constant mixing state index. The addition of the BC particles to the population had a larger impact resulting in a net increase in bulk

diversity and an increased heterogeneity of the particle population. In the last three samples at T0 the particle population then switched to a composition more similar to that observed prior to the buildup event and the mixing state index increased (the population became more homogeneous). Thus, at T0, a change in the particle population was expected based on collocated measurements and the mixing state parameters calculated from the STXM data set showed changes consistent with these expected trends. The mixing state parameterization also provided additional information on the types of particles that comprised the population during the buildup. An increase in soot-dominated particles was observed at T0 which had a large impact on the carbonaceous mixing state of the particle population in these samples.

3.1.3. STXM: BC Mixing State

The changes in the mixing state observed for particles collected at T0 were largely driven by the increase in the soot mass fraction (Figure 3). However, the average particle-specific diversity (D_α) did not increase with the bulk population diversity (D_γ) during the organic buildup, which would be expected if more particles with three components (organic, inorganic, and soot) were added to the population. By excluding all particles that do not contain soot from the data analysis, the mixing state of the soot-containing subpopulation can be investigated, which can give insight into the type of soot particles observed during the buildup event. The number of soot-containing particles was relatively small in both T0 and T1 samples with only 5–20% of the particle number count at T0 and 8–22% of the number count at T1 (Table 1). Given the smaller sample sizes, the statistical significance of the trends is low; the fractional uncertainty of the BC containing particles is on average a factor of 3 higher than for the entire sample. However, the trends match observations for the bulk population and the majority of the samples at T0 have ~100 or more soot-containing particles (Table 1).

Figure 4a shows the trends in average particle-specific diversity, D_α (blue); bulk diversity, D_γ (black); and the mixing state index χ (red) for only particles that contain soot at the T0 site. Figure 4b shows the bulk mass fractions for soot-containing particles from each sample. The temporal series for all three mixing state parameters showed larger ranges, but similar trends, compared to those of the whole population (Figure 3a).

During the period of organic buildup (through 28 June at 15:30) at T0, the bulk diversity, D_γ, increased more than the average particle-specific diversity, D_α, leading to a more heterogeneous particle population (Figures 3a and 4a). Figures 4c and 4d show the mass fractions of individual soot-containing particles in the afternoon before the peak of the organic buildup period (27 June at 12:27) and at the peak of the buildup (28 June at 15:30), respectively. The white line shows the particle-specific diversity, D_i, and the data are plotted according to decreasing BC mass fraction. In the 27 June 12:27 sample (Figure 4c) all but the first ~20 particles had less than one third BC mass fraction. In contrast, for the sample collected on 28 June at 15:30 (Figure 4d) close to half of the particles had one third or more BC mass fraction. Thus, BC dominated particles (BC fraction larger than one third), have increased in number in the 28 June 15:30 (Figure 4d) sample relative to the 27 June 12:27 sample (Figure 4c). This change may be due to the presence of a different source between the two samples or an increased buildup of local emissions. The addition of BC-dominated particles increased D_γ (since the bulk mass fraction of BC is increasing) but did not increase and may even have decreased D_α (since the D_i values were lower). Therefore, an increase in the number of BC-dominated particles contributed to the overall increase in heterogeneity observed in the population during the buildup.

3.1.4. STXM: Diversity as a Function of Size

Figure 5 shows the mass fractions for all particles analyzed from T0 (Figure 5a) and T1 (Figure 5b) samples, plotted as a function of the area equivalent diameter of the impacted particles. The white line shows the particle-specific diversity averaged over each size bin, while the size of the markers shows the number fraction of particles in each size bin (Tables S1 and S2 in the supporting information). Both T0 and T1 have organic and inorganic as the dominant components, with trace black carbon. The mass fractions and the diversity values were relatively constant with size. At T0, a small increase in the average inorganic fraction in the particles with diameters greater than 1 μm was observed; however, this change was within the standard deviation of the other sizes (Table S1).

The relatively constant mass fractions as a function of size at T1 is in contrast with AMS results from T1, which showed a small increase (from 20% to 25%) in the mass fraction of sulfate in larger particles (>300 nm vacuum aerodynamic diameter) [*Setyan et al.*, 2012]. Additionally, the organic mass fractions were lower for the samples discussed here (~50–60%) compared to the particles analyzed at T1 with the AMS (~70–85%) [*Setyan et al.*, 2012]. However, the AMS data for T1 is averaged over the whole campaign, while the data shown in Figure 5 correspond to the average mass fractions from samples collected over only 2 days (Table 2).

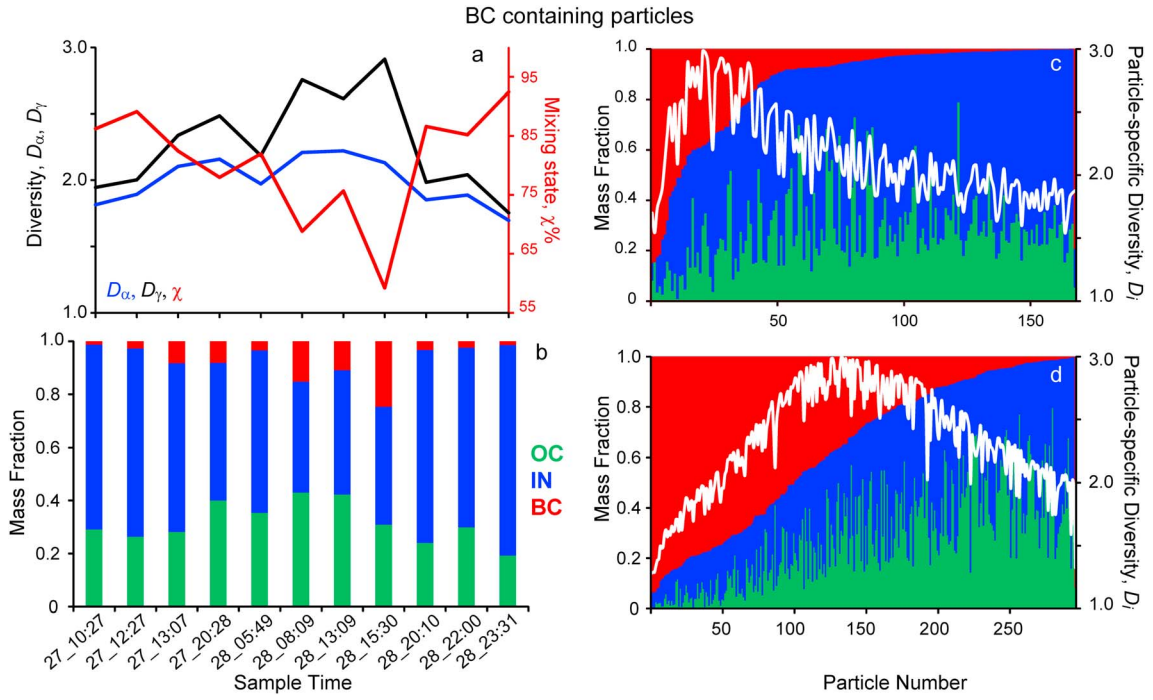

Figure 4. Mixing state parameters and mass fractions for only the T0 particles that contain BC. (a) Average particle-specific, D_α (blue), and bulk, D_γ (black), population diversities, and mixing state index values (red). (b) Bulk mass fractions for each sample. (c and d) Mass fractions per particle and particle-specific diversities (white line) for CARES T0 on 27 June at 12:27 (Figure 4c) and 28 June at 15:30 (Figure 4d).

The relatively constant diversity as a function of size at both T0 and T1 also contrasts with the results reported for the MEGAPOLI campaign [*Healy et al.*, 2014] which showed an increase in D_i with particle diameter due to increased inorganic content in the accumulation mode particles. There, the largest increase in mass fraction was in ammonium nitrate. However, due to the volatility of ammonium nitrate and the fact that both STXM and CCSEM/EDX were run under vacuum, the fraction of ammonium nitrate observed in the microscopy samples is expected to be small [*Richardson and Hightower*, 1987]. In the samples measured here, the major inorganic compounds are expected to be ammonium sulfate, sodium chloride, sodium sulfate, and sodium nitrate. Assuming that the dominant anion in the inorganic is sulfate at both T0 and T1, the results for the inorganic mass fraction here are consistent with the results from MEGAPOLI [*Healy et al.*, 2014], which also showed nearly constant sulfate mass as a fraction of particle size.

For particles from both T0 and T1 samples, the average mass fraction of soot was also relatively constant with size (Figures 5a and 5c). This is in contrast to the results from the MEGAPOLI study [*Healy et al.*, 2014], which showed mass fractions of BC over 30% for particles with aerodynamic diameters less than ~250 nm. The main reasons for this difference are likely (1) the size limit of STXM which had a pixel size of 30 nm and thus a minimum diameter of a little less than 100 nm, (2) different emission characteristics during the MEGAPOLI campaign compared to the 2 days from the CARES campaign discussed here, and (3) the differences in collection efficiency by an impactor sampler; i.e., liquid-like particles are collected more efficiently than solid particles of the same size. Solid particles, such as bare and very thinly coated soot, would be expected to bounce more on impaction than particles which can deform more, like some organic aerosol particles [*Bateman et al.*, 2014]. This difference can affect the mass fractions in favor of particles with more organic and/or inorganic content.

The STXM data sets for both T0 and T1 show constant mass fractions as a function of size (Figure 5). However, the largest uncertainty in these calculations is in the identity of the inorganic components. In the STXM data set, we assume that the inorganic fraction is dominated by ammonium sulfate. In future studies, looking at the inorganic content of the aerosol particle population as a function of size using both CCSEM/EDX and STXM data (at carbon, nitrogen, and oxygen K-edges) on the same particles or at least the same samples would decrease this uncertainty. In the next section, we look at the mixing state of the inorganic fraction from

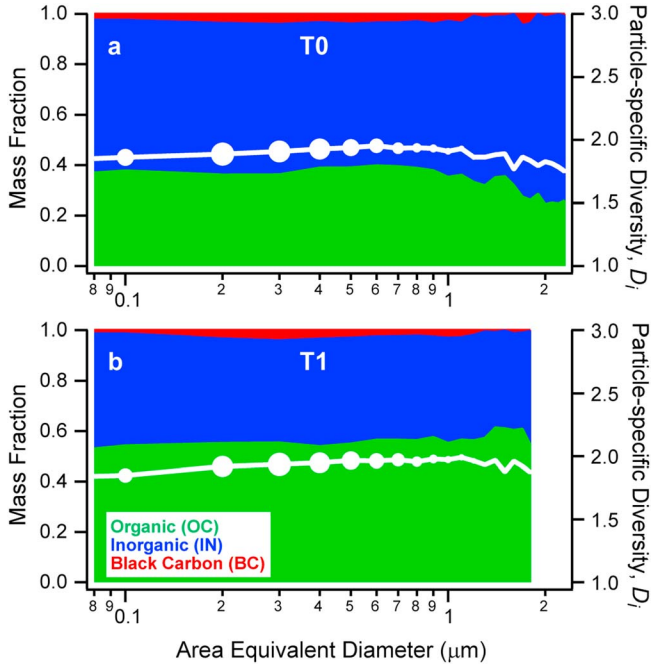

Figure 5. Mass fractions as a function of area equivalent diameter (μm) for (a) T0 and (b) T1. The white line shows the particle-specific diversity value averaged for each size bin and the size of the markers is proportional to the number of particles in that size bin.

CCSEM/EDX analysis of samples collected over the same time range, but not collected at identical sampling times, as the ones discussed above.

3.2. Inorganic Mixing State by CCSEM/EDX

3.2.1. Elemental Masses and Particle Diversities

The STXM data sets discussed previously were collected at the carbon K-edge and provided information on the mixing state of the carbonaceous fraction of aerosol particles at both T0 and T1. Complementary analysis with CCSEM/EDX gives the elemental composition of the particles and can provide detailed information on the inorganic composition. Due to the semiquantitative nature of the lower Z elements [*Laskin et al.*, 2006] we have removed carbon, nitrogen, and oxygen from the mixing state calculations. Thus, we analyze the mixing state with respect to 12 components in the particles (Na, Mg, Al, Si, P, S, Cl, K, Ca, Mn, Fe, and Zn), and the corresponding diversity values can range from 1 (pure particles with 1 component) to 12 (equal mass fractions of all 12 components).

Figures 6a and 6b show the mixing state diagrams for T0 (Figure 6a) and T1 (Figure 6b) from the CCSEM/EDX data set. Two groups of particle populations were observed; four of the samples at T0 (circled in black) had higher average particle-specific diversity and higher mixing state indices than the other samples at T0 and all of the samples at T1. Thus, the range of mixing state indices of particles from T0 was larger, ranging from ~45% to ~90% at T0 versus 41% to 62% at T1. While the degree of internal mixing was high in a few samples (the mixing state index comes close to 100%), the effective number of species is far from the maximum. This is expected due to the fact that 12 elements were measured and particles with equal mass fractions of all 12 elements are unlikely.

Figures 6c and 6d show the mass fractions (bars), the bulk diversity values (solid white line), and the mixing state index (dotted white line) for T0 (Figure 6c) and T1 (Figure 6d) for each of the samples collected on 27 and 28 June. The two types of particle populations were distinguishable in the mass fractions; populations with high Na (and sometimes high Mg and Ca) had higher mixing state parameters and were observed at T0 on 27 June 2010 at 11:47 and 14:27 and on 28 June 2010 at 06:49 and 07:29 (these correspond to the data points circled in Figure 6a). The sulfur dominated samples (>50% mass fraction) had lower mixing state parameters and were observed in the rest of the T0 samples and all of the T1 samples.

Particles in CCSEM/EDX data sets were separated into four particle types based on the percentages of the elements in the particles following particle classification schemes described in *Laskin et al.* [2012]. These four particle types are aged sea salt, aged sea salt with sulfates, carbonaceous, and other. The other category likely includes some particles previously classified as dust, mineral dust, and cooking emissions [*Moffet et al.*, 2013]. Note that since all of the particles in the STXM data set contained some amount of carbon, all of the particle types considered here, including the other group, likely had some carbonaceous content. In *Laskin et al.* [2012], aged sea-salt particles collected during the G-1 flights were found to have a fraction of the Na in the organic phase. Thus, while the CCSEM/EDX provides information on the inorganic content of the aerosol particles, an additional complication arises because Na could be in either the organic or the inorganic phase. Due to the lack of quantification with CCSEM/EDX for carbon, nitrogen, and oxygen, the amount of Na in each phase cannot be calculated. However, future studies that combine STXM/NEXAFS and CCSEM/EDX on the same particles would provide this information.

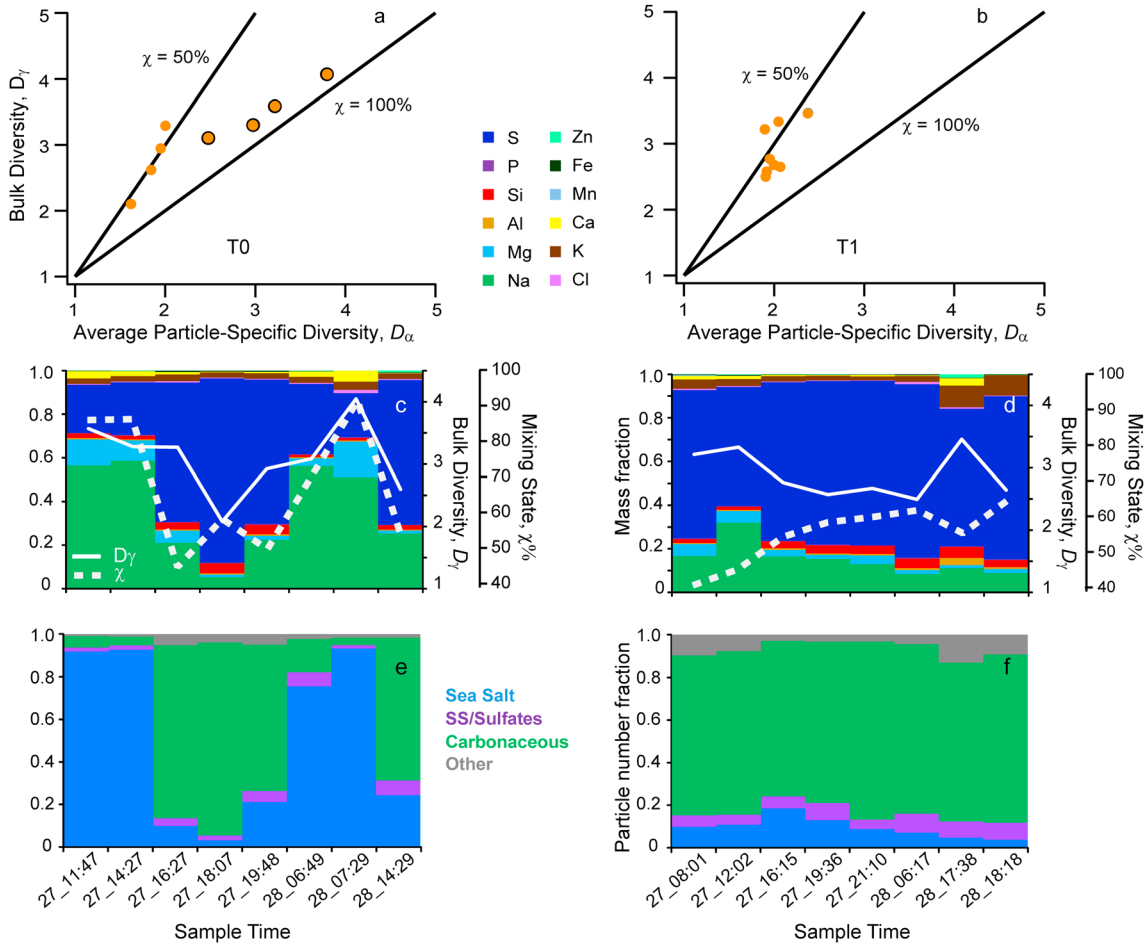

Figure 6. (left column) T0; (right column) T1: (a and b) mixing state diagrams, data are colored orange for clarity; (c and d) mass fractions, bulk diversity values (D_γ, white line), and the mixing state index (χ, dotted white line) for each sample; (e and f) particle number fractions of the four particle types. The color scheme for the elements in Figures 6c and 6d are given between the mixing state diagrams. The circled points in Figure 6a are discussed in the text.

Figures 6e and 6f show the particle number fractions for these four particle types (aged sea salt, aged sea salt with sulfates, carbonaceous, and other) from T0 (Figure 6e) and T1 (Figure 6f) sites as a function of the sample time. At T0, populations with large number fractions of the sea-salt particle type had higher mixing states indices, as well as higher bulk (D_γ) and population diversities (D_α) (Table 2), than populations that were dominated by the carbonaceous particle types. Thus, the populations dominated by aged sea salt were more homogeneous than the populations with more carbonaceous particles.

At T1 the bulk diversity decreased over these 2 days and the mixing state slowly increased (Figure 6d). The one outlier on this trend is the sample collected on 28 June 2010 at 17:38 P.M., which had a higher bulk diversity caused in part by increased mass fractions of K, Ca, Zn, and Al (Figure 6d). This sample also had a larger number of particles in the category other consistent with this sample being potentially influenced by increased amounts of dust and/or food cooking/biomass burning aerosols.

In contrast to T0, the inorganic fraction at T1 became more homogeneous as the fraction of carbonaceous particles increased. The largest mass fraction of sodium was observed at T1 on 27 June 2010 at 12:02, which is within the time frame for direct transport from Sacramento reported by *Fast et al.* [2012]. However, the large mass fractions of Na and the corresponding larger fraction of aged sea-salt particles that were observed in some of the T0 samples were not observed in any of the samples collected at T1. Either the relative abundance of these particles decreased because of emission and formation of carbonaceous particles and thus formed a smaller fraction of the particle population at T1, or, the direct transport of samples with large mass fractions of aged sea salt was not observed in the samples analyzed from T1.

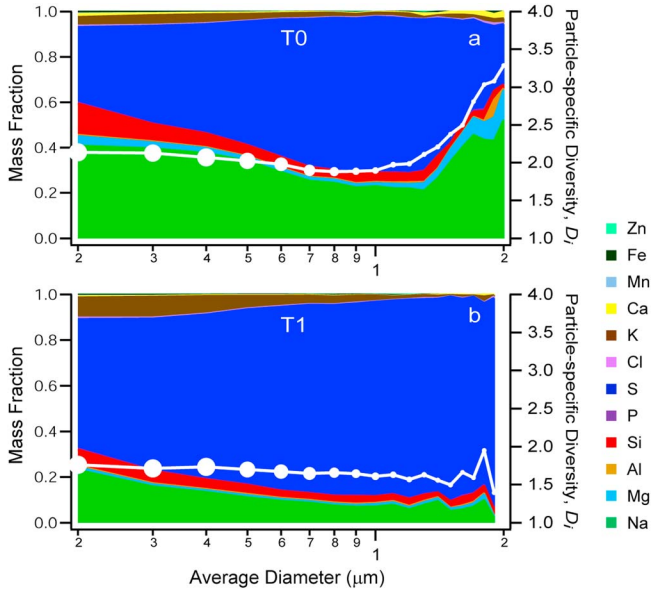

Figure 7. Mass fractions as a function of area equivalent diameter (μm) for (a) T0 and (b) T1. The mass fractions of the elements are stacked in the same order as the key on the right with Na on the bottom. The white line shows the particle-specific diversity value averaged for each size bin, and the marker size is proportional to the number of particles in that size bin.

3.2.2. CCSEM/EDX: Diversity as a Function of Size

Figure 7 shows the mass fractions as a function of size for particles collected at T0 (Figure 7a) and T1 (Figure 7b). The average particle-specific diversity for each size bin is shown by the white line and the size of the markers corresponds to the number of individual particles in that size bin (Tables S3 and S4). The particles collected at T0 had small changes in the mass fractions as a function of size. Sodium had increased mass fractions in the smaller particles ($<$0.5 μm) and the larger particles ($>$1.4 μm). The mass fractions of K, Mg, and Ca appear to show the same trend consistent with the presence of two populations of aged sea-salt particles, one with diameters less than ~600 nm and one with diameters greater than ~1.4 μm. Sulfur was the dominant component ($>$50%) in 0.5–1.5 μm sized particles. An increase in the average diversity was observed in particles $>$1.3 um. However, this increase was only outside of the standard deviation for a few of the larger size bins. The increase in D_i was due to increased mass fractions of the more trace components such as phosphorus, potassium, and calcium in the larger particles.

The particles from T1 had fairly uniform mass fractions and diversity values as a function of size. Compared to T0, the mass fraction of sulfur was larger across all size fractions causing the average diversity value to be lower. This is likely due to increased numbers of organic particles mixed with ammonium sulfate at T1. The particles that contained more Na were in the smaller size fraction. Similar mass fractions were also observed in the smaller particles at T0 consistent with a broadly distributed population of smaller particles, which were potentially fragments of sea-salt (higher Na) and dust (higher Si) particles. The biggest difference in composition between particles collected at T0 and T1 sites is observed for particles in the larger size bins. The larger particles seen at T0 with increased sodium were not observed in the T1 samples, consistent with the lack of direct transport of sea spray emissions to the T1 site, as can be inferred from Figure 6.

4. Conclusions

The analysis presented here is the first application of a new mixing state parameterization to data from single particle spectro-microscopy techniques. The STXM/NEXAFS data collected at the carbon K-edge provided information on the mixing state of the carbonaceous fraction of atmospheric particles, while complementary analysis with CCSEM/EDX provided information on the elemental composition of the inorganic fraction. The parameterization showed changes in the mixing state consistent with results from concurrent measurements and provides additional insights into the types of particles observed in the samples. This analysis used data collected for previous studies [*Knopf et al.*, 2014; *Moffet et al.*, 2013] and did not have direct overlap of the two techniques on the same particles or the same samples. It would be highly advantageous to combine the two techniques on the same particles in future studies. This will provide C, N, O quantification from STXM/NEXAFS and quantification of the inorganic fraction from CCSEM/EDX. Additional analysis that would increase the value of this type of data set include characterizing mixed aerosols of known composition and mass. This work would provide additional validation of the mass estimates used here.

The relatively high mixing state index of the samples analyzed with STXM (>60%) indicates that the particle populations at both field sites during these 2 days were relatively homogeneous with respect to the organic, inorganic, and soot components. The similarity in mixing state indices between T0 and T1 indicates that the increased organic mass fraction at T1 had a small effect on the mixing state of the aerosol population. Based on CCSEM/EDX results, the particle population, which was dominated by aged sea-salt particles [*Laskin et al.*, 2012], showed a relatively high mixing state index, indicating that the aging of sea-salt particles can increase the mixing state index that was calculated based on the inorganic fraction of those particles. Since chloride is depleted while additional sulfate, nitrate, and organic salts are formed in this aging, the increases in the diversity of the inorganic fraction of these particles will likely be enhanced near coastal cities.

More variation in the mixing state parameters was observed for particles collected at the T0 site compared to T1. The smaller variation observed at T1 is consistent with a lack of direct transport from T0 and with an increased amount of particles with high organic and sulfate mass fractions at T1 due to nucleation of new particles and condensational growth. Larger variations in the mixing state at T0 were observed for different reasons in the STXM versus the CCSEM/EDX data sets. For STXM, the variations at T0 were consistent with a buildup event over this time frame; the particle population became more heterogeneous largely due to an increase in the fraction of soot-dominated particles. For CCSEM/EDX, the variations in mixing state observed at T0 were due to the presence of two different types of aerosols. One population was dominated by aged sea-salt particles and was more homogeneous than the other population which was dominated by carbonaceous particles.

The population changes seen in the STXM and CCSEM/EDX data sets do not occur at the same time. More aged sea-salt particles were observed with CCSEM/EDX in the morning samples on both days (Figure 6e), while the soot and organics observed by STXM increased gradually up through the early afternoon of 28 June (Figure 3c). Thus, the two techniques provide complementary information on the mixing state, the sources, and processing of aerosol populations. Analysis of the mass fractions and the mixing states of aerosol particle populations using single particle techniques will be essential to provide constraints upon the results of modeled mixing states.

Acknowledgments

Data supporting all figures are available in Tables S1–S8. Raw image files and codes to process the data are available on request from the corresponding author. This work was supported by the U.S. Department of Energy's Atmospheric System Research, an Office of Science, Office of Biological and Environmental Research program. STXM/NEXAFS was done at beamlines 5.3.2.2 and 11.0.2 at The Advanced Light Source at Lawrence Berkeley National Laboratory, which are supported by the Director, Office of Science, Office of Basic Energy Sciences, (beamline 11.0.2 is also supported by the Division of Chemical Sciences, Geosciences, and Biosciences) of the U.S. Department of Energy under contract DE-AC02-05CH11231. CCSEM/EDX analysis of particles was performed at Environmental Molecular Sciences Laboratory, a national scientific user facility sponsored by OBER at Pacific Northwest National Laboratory. PNNL is operated by the U.S. Department of Energy by Battelle Memorial Institute under contract DE-AC06-76RL0. Q.Z. and Y.S. would like to acknowledge funding from DE-FG02-11ER65293. We wish to acknowledge the continued support of A.L.D Kilcoyne and T. Tyliszczak for their support on the STXM instruments. We also wish to acknowledge the support of Nels Laulainen for assistance with the collection of Sunset ECOC data and Celine Kluzek for assistance with the collection of PILS data.

References

Bateman, A. P., H. Belassein, and S. T. Martin (2014), Impactor apparatus for the study of particle rebound: Relative humidity and capillary forces, *Aerosol Sci. Technol.*, *48*(1), 42–52.

Bond, T. C., and R. W. Bergstrom (2006), Light absorption by carbonaceous particles: An investigative review, *Aerosol Sci. Technol.*, *40*(1), 27–67.

Bond, T. C., et al. (2013), Bounding the role of black carbon in the climate system: A scientific assessment, *J. Geophys. Res. Atmos.*, *118*, 5380–5552, doi:10.1002/jgrd.50171.

Cappa, C. D., et al. (2012), Radiative absorption enhancements due to the mixing state of atmospheric black carbon, *Science*, *337*(6098), 1078–1081.

Fast, J. D., et al. (2012), Transport and mixing patterns over Central California during the Carbonaceous Aerosol and Radiative Effects Study (CARES), *Atmos. Chem. Phys.*, *12*(4), 1759–1783.

Healy, R. M., et al. (2014), Single particle diversity and mixing state measurements, *Atmos. Chem. Phys.*, *14*(12), 6289–6299.

Henke, B. L., E. M. Gullikson, and J. C. Davis (1993), X-ray interactions: Photoabsorption, scattering, transmission and reflection at E = 50–30,000 eV, Z = 1–92 (VOL 54, PG 181, 1993), *Atom. Data Nucl. Data Tables*, *55*(2), 349–349.

Hopkins, R. J., K. Lewis, Y. Desyaterik, Z. Wang, A. V. Tivanski, W. P. Arnott, A. Laskin, and M. K. Gilles (2007), Correlations between optical, chemical and physical properties of biomass burn aerosols, *Geophs. Res. Lett.*, *34*, L18806, doi:10.1029/2007GL030502.

Jacobson, M. C., H. C. Hansson, K. J. Noone, and R. J. Charlson (2000), Organic atmospheric aerosols: Review and state of the science, *Rev. Geophys.*, *38*(2), 267–294, doi:10.1029/1998RG000045.

Jacobson, M. Z. (2001), Strong radiative heating due to the mixing state of black carbon in atmospheric aerosols, *Nature*, *409*(6821), 695–697.

Johnson, K. S., B. Zuberi, L. T. Molina, M. J. Molina, M. J. Iedema, J. P. Cowin, D. J. Gaspar, C. Wang, and A. Laskin (2005), Processing of soot in an urban environment: Case study from the Mexico City Metropolitan Area, *Atmos. Chem. Phys.*, *5*, 3033–3043.

Kanakidou, M., et al. (2005), Organic aerosol and global climate modelling: A review, *Atmos. Chem. Phys.*, *5*, 1053–1123.

Kilcoyne, A. L. D., et al. (2003), Interferometer-controlled scanning transmission X-ray microscopes at the Advanced Light Source, *J. Synchrotron Rad.*, *10*, 125–136.

Knopf, D. A., B. Wang, A. Laskin, R. C. Moffet, and M. K. Gilles (2010), Heterogeneous nucleation of ice on anthropogenic organic particles collected in Mexico City, *Geophys. Res. Lett.*, *37*, L11803, doi:10.1029/2010GL043362.

Knopf, D. A., P. A. Alpert, B. Wang, R. E. O'Brien, S. T. Kelly, A. Laskin, M. K. Gilles, and R. C. Moffet (2014), Microscpectriscopic imaging and characterization of individually identified ice nucleating particles from a case field study, *J. Geophys. Res. Atmos.*, *119*, 10,365–10,381, doi:10.1002/2014JD021866.

Lack, D. A., J. M. Langridge, R. Bahreini, C. D. Cappa, A. M. Middlebrook, and J. P. Schwarza (2012), Brown carbon and internal mixing in biomass burning particles, *Proc. Natl. Acad. Sci. U.S.A.*, *109*(37), 14,802–14,807.

Laskin, A., M. J. Iedema, and J. P. Cowin (2003), Time-resolved aerosol collector for CCSEM/EDX single-particle analysis, *Aerosol Sci. Technol.*, *37*(3), 246–260.

Laskin, A., J. P. Cowin, and M. J. Iedema (2006), Analysis of individual environmental particles using modern methods of electron microscopy and X-ray microanalysis, *J. Electron Spectrosc. Relat. Phenom.*, *150*(2–3), 260–274.

Laskin, A., R. C. Moffet, M. K. Gilles, J. D. Fast, R. A. Zaveri, B. Wang, P. Nigge, and J. Shutthanandan (2012), Tropospheric chemistry of internally mixed sea salt and organic particles: Surprising reactivity of NaCl with weak organic acids, *J. Geophys. Res. 117*, D15302,doi:10.1029/2012JD017743.

MacKay, D. J. C. (2003), *Information Theory, Inference, and Learning Algorithms*, Cambridge Univ. Press, Cambridge, U. K.

Mikhailov, E. F., S. S. Vlasenko, I. A. Podgorny, V. Ramanathan, and C. E. Corrigan (2006), Optical properties of soot-water drop agglomerates: An experimental study, *J. Geophys. Res.*, *111*, D07209, doi:10.1029/2005JD006389.

Moffet, R. C., and K. A. Prather (2009), In-situ measurements of the mixing state and optical properties of soot with implications for radiative forcing estimates, *Proc. Natl. Acad. Sci. U.S.A.*, *106*(29), 11,872–11,877.

Moffet, R. C., T. Henn, A. Laskin, and M. K. Gilles (2010a), Automated chemical analysis of internally mixed aerosol particles using X-ray spectromicroscopy at the carbon K-edge, *Anal. Chem.*, *82*(19), 7906–7914.

Moffet, R. C., et al. (2010b), Microscopic characterization of carbonaceous aerosol particle aging in the outflow from Mexico City, *Atmos. Chem. Phys.*, *10*(3), 961–976.

Moffet, R. C., A. V. Tivanski, and M. K. Gilles (2011), Scanning transmission X-ray microscopy applications in atmospheric aerosol research, in *Fundamentals and Applications in Aerosol Spectroscopy*, edited by R. Signorell and J. P. Reid, pp. 434–436, CRC Press, Taylor & Francis Group, Boca Raton, Fla.

Moffet, R. C., T. C. Roedel, S. T. Kelly, X. Y. Yu, G. T. Carroll, J. Fast, R. A. Zaveri, A. Laskin, and M. K. Gilles (2013), Spectro-microscopic measurements of carbonaceous aerosol aging in Central California, *Atmos. Chem. Phys.*, *13*(20), 10,445–10,459.

O'Brien, R. E., A. Neu, S. A. Epstein, A. C. MacMillan, B. Wang, S. T. Kelly, S. A. Nizkorodov, A. Laskin, R. C. Moffet, and M. K. Gilles (2014), Physical properties of ambient and laboratory-generated secondary organic aerosol, *Geophys. Res. Lett.*, *41*, 4347–4353, doi:10.1002/2014GL060219.

Petters, M. D., and S. M. Kreidenweis (2007), A single parameter representation of hygroscopic growth and cloud condensation nucleus activity, *Atmos. Chem. Phys.*, *7*(8), 1961–1971.

Poschl, U. (2005), Atmospheric aerosols: Composition, transformation, climate and health effects, *Angew. Chem. Int. Ed.*, *44*(46), 7520–7540.

Richardson, C. B., and R. L. Hightower (1987), Evaporation of ammonium-nitrate particles, *Atmos. Environ.*, *21*(4), 971–975.

Riemer, N., and M. West (2013), Quantifying aerosol mixing state with entropy and diversity measures, *Atmos. Chem. Phys.*, *13*(22), 11,423–11,439.

Saleh, R., et al. (2014), Brownness of organics in aerosols from biomass burning linked to their black carbon content, *Nat. Geosci.*, *7*(9), 647–650.

Schnaiter, M., C. Linke, O. Mohler, K.-H. Naumann, H. Saathoff, R. Wagner, U. Schurath, and B. Wehner (2005), Absorption amplification of black carbon internally mixed with secondary organic aerosol, *J. Geophys. Res.*, *110*, D19204, doi:10.1029/2005JD006046.

Seinfeld, J. H., and S. N. Pandis (2006), *Atmospheric Chemistry and Physics: From Air Pollution to Climate Change*, John Wiley & Sons, Inc., Hoboken N. J.

Setyan, A., et al. (2012), Characterization of submicron particles influenced by mixed biogenic and anthropogenic emissions using high-resolution aerosol mass spectrometry: Results from CARES, *Atmos. Chem. Phys.*, *12*(17), 8131–8156.

Setyan, A., C. Song, M. Merkel, W. B. Knighton, T. B. Onasch, M. R. Canagaratna, D. R. Worsnop, A. Wiedensohler, J. E. Shilling, and Q. Zhang (2014), Chemistry of new particle growth in mixed urban and biogenic emissions—Insights from CARES, *Atmos. Chem. Phys.*, *14*(13), 6477–6494.

Solomon, S., D. Qin, M. Manning, Z. Chen, M. Marquis, K. B. Averyt, M. Tignor, and H. L. Miller (2007), *IPCC, 2007: Climate Change 2007: The Physical Science Basis. Contribution of Working Group I to the Fourth Assessment Report of the Intergovernmental Panel on Climate Change*, Cambridge Univ. Press, Cambridge, U. K., and New York.

Wang, B. B., A. Laskin, T. Roedel, M. K. Gilles, R. C. Moffet, A. V. Tivanski, and D. A. Knopf (2012), Heterogeneous ice nucleation and water uptake by field collected atmospheric particles below 273 K, *J. Geophys. Res.*, *117*, D00V19, doi:10.1029/2012JD017446.

Wang, J., M. J. Cubison, A. C. Aiken, J. L. Jimenez, and D. R. Collins (2010), The importance of aerosol mixing state and size-resolved composition on CCN concentration and the variation of the importance with atmospheric aging of aerosols, *Atmos. Chem. Phys.*, *10*(15), 7267–7283.

Zaveri, R. A., et al. (2012), Overview of the 2010 Carbonaceous Aerosols and Radiative Effects Study (CARES), *Atmos. Chem. Phys.*, *12*(16), 7647–7687.

Zelenay, V., et al. (2011), Aging induced changes on NEXAFS fingerprints in individual combustion particles, *Atmos. Chem. Phys.*, *11*(22), 11,777–11,791.